Attosecond spectral singularities in solid-state high-harmonic generation

Uzan, Ayelet Julie; Orenstein, Gal; Jimenez-Galan, Alvaro

Uzan, A. J., Orenstein, G., Jimenez-Galan, A., McDonald, C., Silva, R. E. F., Bruner, B. D., Klimkin, N. D., Blanchet, V., Arusi-Parpar, T., Krueger, M., Rubtsov, A. N., Smirnova, O., Ivanov, M., Yan, B., Brabec, T., & Dudovich, N. (2020). Attosecond spectral singularities in solid-state high-harmonic generation. Nature Photonics, 14(3), 183–187. https://doi.org/10.1038/s41566-019-0574-4
Document Version: Accepted

Published Version: https://doi.org/10.1038/s41566-019-0574-4

Query Details

Back to Main Page

1. Please provide an email address for author 'Nirit Dudovich'

nirit.dudovich@weizmann.ac.il

2. Please check that the abstract is OK as edited.

The abstract is great. Just a small correction in the first sentence (which I already marked)- we refer to electric currents dreiven by a strong field, so the hyphen should be between the "strong" and the "field".

3. Please check your article carefully, coordinate with any co-authors and enter all final edits clearly in the eproof, remembering to save frequently. Once corrections are submitted, we cannot routinely make further changes to the article.

Done. Thanks.

4. Note that the eproof should be amended in only one browser window at any one time; otherwise changes will be overwritten.

Noted.

5. Author surnames have been highlighted. Please check these carefully and adjust if the first name or surname is marked up incorrectly. Note that changes here will affect indexing of your article in public repositories such as PubMed. Also, carefully check the spelling and numbering of all author names and affiliations, and the corresponding email address(es).

Done

6. You cannot alter accepted Supplementary Information files except for critical changes to scientific content. If you do resupply any files, please also provide a brief (but complete) list of changes. If these are not considered scientific changes, any altered Supplementary files will not be used, only the originally accepted version will be published.

No need to change anything in the supplementary.

7. Please note - to comply with journal style, panel e in Figure 1 is now treated as an inset to Figure 1b. Please check that all mentions of Figure 1b and e (was f) are correct.

checked.

8. Figure 1 - please check that the mention of Supplementary equations is correct.

The mention is correct.

9. Please note that panel a of Figure 2 has been moved to the left of panels b and d, to comply with journal style.

o.k.

10. Please check that all equations are correct as transcribed.

Checked.

11. If ref. 32 (preprint) has now been published in final peer-reviewed form, please update the reference details if appropriate.

It has not been published yet.

Attosecond spectral singularities in solid-state high harmonic generation

Ayelet Julie Uzan, [1]

Gal Orenstein, [1]✉

Email gal.orenstein@weizmann.ac.il

Álvaro Jiménez-Galán, [2]

Chris McDonald, [3]

Rui E. F. Silva, [4]

Barry D. Bruner, [1]

Nikolai D. Klimkin, [5,6]

Valerie Blanchet, [7]

Talya Arusi-Parpar, [1]

Michael Krüger, [1]

Alexey N. Rubtsov, [5,6]

Olga Smirnova, [2,8]

Misha Ivanov, [2,9,10]

Binghai Yan, [11]

Thomas Brabec, [3]

Nirit Dudovich, [1]

[1] Department of Complex Systems, Weizmann Institute of Science, Rehovot, Israel

[2] Max-Born-Institut, Berlin, Germany

[3] Department of Physics, University of Ottawa, Ottawa, Ontario, Canada

[4] Department of Theoretical Condensed Matter Physics, Universidad AutÃşnoma de Madrid, Madrid, Spain

[5] Russian Quantum Center, Skolkovo, Russia

[6] Department of Physics, Moscow State University, Moscow, Russia

[7] Université de Bordeaux–CNRS, CELIA, Talence, France

[8] Technische Universität Berlin, Berlin, Germany

[9] Blackett Laboratory, Imperial College London, London, UK

[10] Department of Physics, Humboldt University, Berlin, Germany

[11] Department of Condensed Matter Physics, Weizmann Institute of Science, Rehovot, Israel

Received: 11 November 2018 / Accepted: 1 December 2019

Abstract

Strong-–field-driven electric currents in condensed matter systems are opening new frontiers in petahertz electronics. In this regime, new challenges are arising as the roles of band structure and coherent electron–hole dynamics have yet to be resolved. Here, by using high harmonic generation spectroscopy, we reveal the underlying attosecond dynamics that dictates the temporal evolution of carriers in multi-band solid-state systems. We demonstrate that when the electron–hole

relative velocity approaches zero, enhanced constructive interference leads to the appearance of spectral caustics in the high harmonic generation spectrum. We introduce the role of the dynamical joint density of states and identify its mapping into the spectrum, which exhibits singularities at the spectral caustics. By studying these singularities, we probe the structure of multiple unpopulated high conduction bands.

AQ1

AQ2

Editor's Summary

High harmonic waves are generated from a MgO crystal under experimental condition where the simple semi-classical analysis fails. The high harmonic generation spectroscopy directly probes the strong-field attosecond dynamics over multiple bands.

These authors contributed equally: Ayelet Julie Uzan, Gal Orenstein.

Main

Induced by the strong-field interaction, high harmonic generation (HHG) provides a unique spectroscopic scheme to visualize the coherent evolution of petahertz currents inside solids. Since it was first observed[1], solid-state HHG has opened a door into studies of the electronic structure and dynamics in crystals[2, 3, 4, 5, 6, 7] as well as the multiple band dynamics[8, 9, 10, 11] and complex many-body phenomena[12] in crystalline and amorphous systems[9]. For a moderate field strength, the electron–hole dynamics are often described semiclassically by a single pair of valence and conduction bands. As we approach the strong-field regime, new fundamental questions arise. What is the role of the band structure in such intense, ultrafast processes? How does the coherent electron–hole dynamics evolve over extremely short timescales? These questions pose some of the primary challenges in the emerging field of strong-field interactions in solids.

AQ3

AQ4

AQ5

AQ6

In this Article we identify the quantum characteristics of the electron–hole wave packet in solids where the simple semi-classical analysis[13] fails, probing its

strong-field attosecond dynamics over multiple bands. We observe enhanced constructive interference in the vicinity of Van Hove singularities[14, 15] and resolve the link between the dynamical joint density of states (JDOS) and the HHG spectrum. Our study applies HHG spectroscopy in MgO, driven by a $\lambda = 1.3$ μm laser field at around 1×10^{13} W cm^{-2} intensity. Adding a weak perturbative second harmonic field modulates the internal dynamics, in close analogy to a lock-in measurement. This scheme allows us to isolate extremely weak signals and identify the contribution of multiple band excitations, covering a spectral range up to 30 eV. Our results show unequivocally that the internal dynamics related to HHG in this system are dominated by the inter-band emission[1, 3, 4, 7],[16, 17, 18, 19, 20, 21, 22], which remains the dominant mechanism when higher conduction bands are involved. We identify the mapping between the dynamical JDOS at unique regions in the Brillouin zone (BZ) and the HHG spectrum. At Van Hove singularities, spectral caustics are induced, leading to a strong enhancement of the HHG signal. At these critical points, the description of the underlying dynamics requires a comprehensive quantum analysis, as given by catastrophe theory[23, 24].

Inter-band emission

The inter-band HHG mechanism can be viewed as a generalized electron–hole recollision process[16, 20], described by a semi-classical analysis[13]. Around the peak of the laser field, an electron tunnels from the valence to the conduction band, forming an electron–hole pair. The laser field subsequently accelerates the pair, leading to their recombination and the emission of extreme ultraviolet (XUV) radiation. This model maps the semi-classical electron–hole trajectories into harmonic energies. The semi-classical analysis is not strictly limited to one conduction band—the strong laser field may excite the electron into higher bands, leading to the generation of complex spectral features in the HHG spectrum[8, 9, 10].

A fundamental aspect of the HHG inter-band dynamics is the localization of the excited electron–hole wave packet in the BZ around the minimum bandgap at the instant of tunnelling. As the wave packet evolves under the influence of the laser field, it dynamically probes a narrow stripe of the BZ along the field's polarization, as illustrated in Fig. 1a. Such localization is a key property of HHG spectroscopy, enabling visualization of the band structure with a unique angular resolution.

Fig. 1

HHG spectroscopy in MgO.

a, Schematic description of three snapshots (green, blue and cyan) at different times of the electron–hole coherence, which leads to the inter-band emission (Supplementary equations (1) and (7)). As the electron and hole propagate, their coherence probes a narrow stripe of the BZ on the bandgap (represented by the surface), along the laser polarization (red line). **b**–**d**, Normalized oscillating HHG spectrum (cyan) and normalized averaged spectrum (violet) in logarithmic scale for orientations 0° (**b**), 33° (**c**) and 45° (**d**). The two spectra are vertically shifted to allow better visibility. Inset: the crystal is oriented to angle θ with respect to the fundamental field's polarization (red arrow) while the second harmonic (blue arrow) is orthogonally polarized. **e**, Electron–hole trajectories, represented by arrows, propagating along the bandgap. Their recombination maps the bandgap into the emission of high harmonics. Around the extrema of the bandgap, the dynamics is dictated by the constructive interference of many trajectories. At these points the semi-classical mapping fails, leading to the appearance of spectral caustics.

AQ8

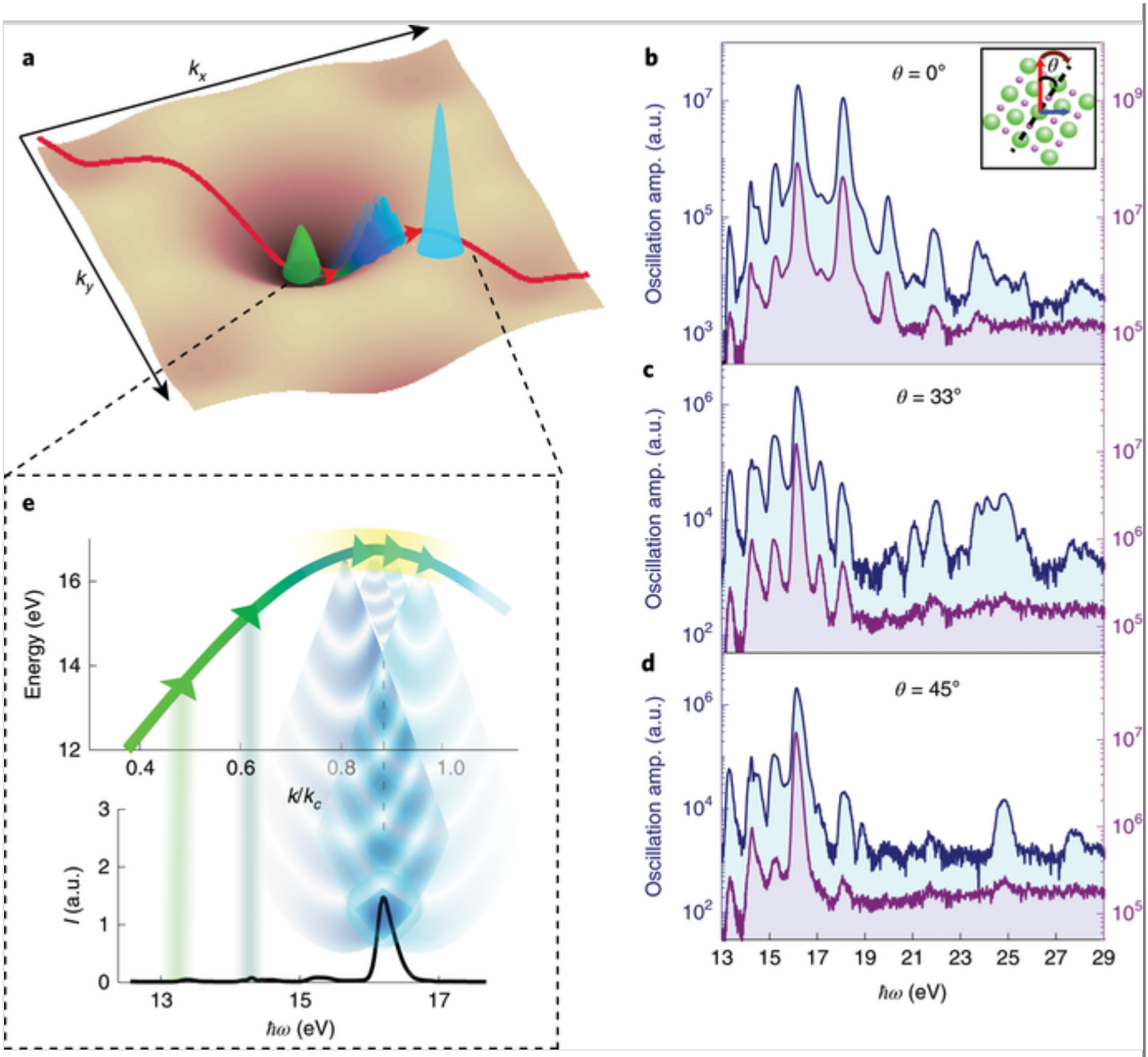

AQ7

Results

Two-colour lock-in measurement

Resolving the angular dependence of the HHG spectrum is challenging—the HHG signal drops rapidly when the polarization is rotated off the main axes of the MgO crystal[25]. Such suppression becomes even more significant when the harmonics are produced from higher conduction bands[26]. To fully reveal the electron–hole dynamics, both its angular dependence as well as the contribution of multiple bands, we introduce an advanced measurement scheme that enables us to resolve and isolate the weak HHG signals while probing its dynamical properties.

Enhancing the detectability of weak signals by subjecting them to a known temporal modulation is a common practice in a wide range of applications, and is also known as lock-in measurement. We induce such a modulation by adding a weak second harmonic field polarized perpendicular to the polarization of the fundamental field. So far, this scheme has been applied to probe the internal dynamics in gas-phase HHG[27] and inter-band currents within the first conduction band of ZnO[16]. Scanning the two-colour delay leads to a periodic modulation of the HHG spectrum with four times the frequency of the fundamental laser. Fourier analysis isolates the oscillating component, resolving the weak HHG signals buried in a large experimental background (Supplementary Fig. 1). In addition, XUV emission from higher conduction bands can be highly sensitive to the two-colour delay[28], resulting in an enhanced signature in the oscillating component. Figure 1b–d compares the oscillating component of the HHG signal at four times the fundamental laser frequency and the spectra averaged over the two-colour delay for crystal orientations of 0°, 33° and 45°, respectively (Fig. 1b, inset). These spectra were normalized for each angle independently (see the complete angular dependence in Supplementary Fig. 2). Clearly, the averaged spectrum is accompanied by large background noise and is dominated by harmonic 17 (~16.2 eV) for 33° and 45° and harmonics 17 and 19 (~18.1 eV) for 0°. Resolving the oscillating spectrum by Fourier analysis shows a dramatic enhancement of the signal over the noise. This measurement shows the appearance of new spectral components that were previously hidden in the averaged spectrum.

Spectral caustics at Van Hove singularities

The oscillating spectra reveal that, for all crystal angles, the spectrum extends beyond the first band edge (~18 eV, Fig. 2a), indicating the strong contribution of higher conduction bands. The most important observation is associated with the angular dependence of the measurement—the oscillating spectrum varies drastically for different angles, exhibiting enhanced features and structures over a wide spectral range. We identify three distinct structures: enhanced harmonics around 16–17 eV extending to 18 eV at 0°, an increased signal in the 20.5–22.5 eV region at 33° and a clear spectral feature at 23.5–26 eV. What is the origin of the enhancement mechanism in these spectral regions and what information does it provide?

Fig. 2

Spectral caustics at singular points of the dynamical JDOS.

a, The band structure along the 0° (Γ–X) and 45° (Γ–K) orientations. The dashed line is the valence band and the coloured lines are the conduction bands, which are dipole-coupled to the valence band. The grey bands indicate the existing bands, which are not dipole-coupled. **b**,**c**, Plots of $\nabla_{\mathbf{k}}\varepsilon_{\mathrm{g}}(\mathbf{k})$ along 0° (**b**) and 45° (**c**), respectively. The energies for which $\nabla_{\mathbf{k}}\varepsilon_{\mathrm{g}}(\mathbf{k}) = 0$ are indicated by circled numbers, which are mapped to the corresponding points in **a**. **d**,**e**, The oscillating spectra at 0° (**d**) and 45° (**e**), respectively. The energies for which singularities in the dynamical JDOS occur are highlighted by corresponding coloured bars, emphasizing their link to the spectral caustics. The oscillating spectra in **d** and **e** are split into two parts separated by vertical dotted lines. The spectra to the right of the dotted lines are enhanced by a factor of 50 (as indicated above the arrow) for better visibility.

AQ9

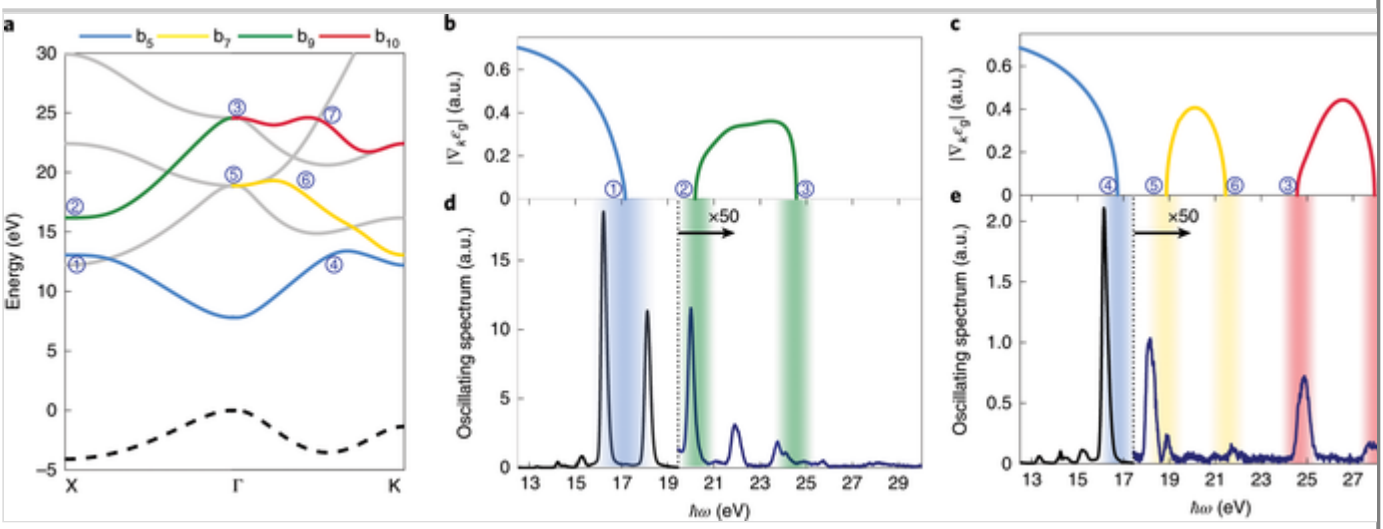

We start by analysing the enhancement at 23.5–26 eV. The observation is striking—clearly, this spectral region originates from a high conduction band excitation associated with a low population transfer. Furthermore, although the oscillating spectrum changes dramatically with the crystal orientation, this feature remains robust. This suggests that it originates from areas of the BZ that are orientation-independent. These areas can be found around the Γ point of the BZ, which is common to all crystal orientations. Figure 2a shows the band structure for crystal orientations of 0° and 45° (Γ–X and Γ–K, respectively). Indeed, we find two high conduction bands intersecting the Γ point at an energy of 24.57 eV. At the Γ point these bands, as well as any other band, have a critical point, $\nabla_{\mathbf{k}}E_{\mathrm{c}}(\mathbf{k}) = \nabla_{\mathbf{k}}E_{\mathrm{v}}(\mathbf{k}) = 0$, such that the gradient of the energy gap is zero as well:

$$\nabla_{\mathbf{k}}\left(E_{\mathrm{c}}(\mathbf{k}) - E_{\mathrm{v}}(\mathbf{k})\right) = \nabla_{\mathbf{k}}\varepsilon_{\mathrm{g}}(\mathbf{k}) = 0 \qquad 1$$

where $\mathbf{k}$ is the lattice momentum, E_c is the conduction band and E_v is the valence band. At these points, the relative semi-classical velocity between the electron ($\nabla_{\mathbf{k}} E_c$) and the hole ($\nabla_{\mathbf{k}} E_v$) vanishes, leading to a significant enhancement in their recombination rate.

AQ10

To appreciate how the gradient of the energy gap affects the HHG signal we examine the quantum-mechanical expression for the inter-band currents[13, 20]:

$$\mathbf{j}_{er}(\omega) = \omega \int_{BZ} \mathrm{d}^3\mathbf{k} \iint \mathbf{g}(\mathbf{k}, t', t) \exp^{-iS(\mathbf{k},t',t)+i\omega t} \mathrm{d}t\mathrm{d}t' \quad (2)$$

$$S(\mathbf{k}, t', t) = \int_{t'}^{t} \varepsilon_g(\mathbf{k} - \mathbf{A}(t) + \mathbf{A}(\tau))\mathrm{d}\tau \quad (3)$$

where $\mathbf{A}$ is the vector potential and ω is the harmonic energy. $\mathbf{g}(\mathbf{k}, t', t)$ represents a slowly varying term compared to the rapidly oscillating exponential containing the semi-classical action, $S(\mathbf{k}, t', t)$. Under these conditions, the largest contributions to the integral in equation (2) will come from constructive interference around points where the phase, $S(\mathbf{k}, t', t)$, is stationary. These stationary points define the semi-classical mapping between harmonic energy and recolliding electron and hole trajectories. The inter-band current for a single stationary solution, as obtained from the stationary phase approximation (SPA), is proportional to $\sqrt{|\hat{\mathbf{S}}''(\mathbf{k}_{st}, t'_{st}, t_{st})|}^{-1}$, where $\hat{\mathbf{S}}''(\mathbf{k}_{st}, t'_{st}, t_{st})$ is the Hessian matrix of the function $S(\mathbf{k},t',t)$ at the stationary points. This derivation directly links the HHG spectrum and the band structure (for a detailed derivation see Supplementary Information):

$$|\hat{\mathbf{S}}''(\mathbf{k}_{st}, t'_{st}, t_{st})| \propto |\nabla_{\mathbf{k}} \varepsilon_g(\mathbf{k}_{st})| \quad (4)$$

$$I(\omega) \propto |\mathbf{j}_{er}(\omega)|^2 \propto \omega^2 \left| \sum\nolimits_{\mathbf{k}_{st}} \frac{\tilde{\mathbf{g}}(\mathbf{k}_{st}, t'_{st}, t_{st}) \mathrm{e}^{-iS(\mathbf{k}_{st}, t'_{st}, t_{st})}}{\sqrt{|\nabla_{\mathbf{k}} \varepsilon_g(\mathbf{k}_{st})|}} \right|^2 \quad (5)$$

where $\varepsilon_g(\mathbf{k}_{st})$ is the energy difference between electron and hole at the time of recollision, which defines the harmonic energy, and $\tilde{\mathbf{g}}$ accounts for all pre-exponential terms. The exponent in equation (5) describes the quantum phase and

amplitude associated with each trajectory. Due to strong-field tunnelling, the quantum amplitude is strongly attenuated with increasing $|\mathbf{k}_{\mathrm{st}}^{\perp}|$, where $\mathbf{k}_{\mathrm{st}}^{\perp}$ is the component of $\mathbf{k}_{\mathrm{st}}$ perpendicular to the laser's polarization. Such attenuation reflects that the HHG signal indeed originates from a narrow stripe of the BZ along the laser polarization, providing the significant angular dependence of the spectrum.

The expression for the spectral intensity (equation (5)) strongly resembles that of the JDOS, differing only by the fact that the summation is discrete and weighted by the exponent of the semi-classical action. Due to the temporal properties of the action, we associate the spectral intensity with a dynamical JDOS. At the critical points of the bandgaps, the JDOS of a crystalline solid becomes singular. These singularities are known as Van Hove singularities[15] and most commonly arise in the analysis of optical absorption and reflection spectra[29, 30]. However, in contrast to the JDOS of three-dimensional (3D) materials, which exhibits square-root singularities[15] analogous to the DOS of a 3D free-electron gas, the dynamical JDOS explicitly diverges when $\nabla_{\mathbf{k}}\varepsilon_{\mathrm{g}}(\mathbf{k}_{\mathrm{st}}) = 0$. At these unique points the Hessian matrix becomes singular, according to equation (4). Consequentially, the semi-classical action is stationary to higher than first order, leading to an enhanced constructive interference of the inter-band currents (equation (2)). As a result, the simple semi-classical model fails to quantitatively describe these currents, instead requiring a comprehensive quantum description.

The singularities in the mapping between harmonic energy and electron–hole trajectories can be described within the framework of caustics[23]. Caustics are universal phenomena in nature that link processes observed in many different branches of physics. Previous studies identified the appearance of caustics in gas-phase HHG[23, 31], where they reveal the quantum nature of the process in a regime where a semi-classical analysis fails. Figure 1e illustrates the origin of spectral caustics in condensed matter systems. Far from the singularities, electron–hole dynamics is dominated by the semi-classical trajectories. However, around the extrema of the bandgap, where the electron–hole wave packet has zero relative velocity, the dynamics is dictated by the constructive interference of many trajectories. At these points, the semi-classical mapping fails, leading to the appearance of spectral caustics.

The enhancement at 23.5–26 eV can be identified as a spectral caustic originating from the singularity at the Γ point (Fig. 2). Another energy band intersecting the Γ point can be found at 18.8 eV, leading to a robust spectral feature near 18 eV, as can be seen in Fig. 1b–d. Although the crossing of energy bands at the Γ point will

always result in singularities, spectral caustics can be found at other points in the BZ as well. Along the high-symmetry axes of the crystal, 0° and 45°, each bandgap exhibits several critical points where $\nabla_{\mathbf{k}}\varepsilon_{\mathrm{g}}(\mathbf{k}_{\mathrm{st}}) = 0$. In Fig. 2 we show how these points are imprinted in the experimentally resolved HHG spectrum. Figure 2b,c describes the gradient of each bandgap as a function of the bandgap energy, for crystal orientations of 0° and 45°, respectively. Figure 2d,e presents the measured oscillating spectra at these angles. The highlighted lines in Fig. 2d,e emphasize the energy points where the gradient is zero and the dynamical JDOS becomes singular according to equation (5). Indeed, caustics dominate the brightest features of the HHG spectrum, leading to a dramatic spectral focusing and enhancement of the weak signal associated with the excitation of higher conduction bands.

Angular and temporal properties of the caustic harmonics

The caustic harmonics in condensed matter systems exhibit distinct angular and temporal properties. Catastrophe theory classifies the different caustics according to the dimensionality of the mapping and the number of control parameters, predicting their basic characteristics[24]. In our experiment we have one control parameter, the orientation of the crystal, so the caustics we observe are classified as ‘fold’ catastrophes. Catastrophe theory predicts that the ‘fold’ enhancement should exhibit a spectral and angular Airy function dependence. Resolving the angular dependence enables us to sample the caustic’s shape with high resolution, as we are not limited by the discrete nature of the harmonics. We extract the angular dependence of the harmonics at 16.2, 18.1, 20 and 22 eV, dividing their intensity by that of the harmonic at 14.3 eV, which is spectrally located far from the singularities. Figure 3a presents the angular dependence for the 16.2 and 18.1 eV harmonics (purple and blue circles, respectively), while ~~the inset (~~Fig. 3b It is no longer an inset. ~~)~~ presents this dependence for the 20 and 22 eV ones. We focus on a narrow angular range that predominantly exhibits caustic contributions originating from the 0° critical points. The harmonics at 16.2, 18.1 and 20 eV exhibit the typical Airy attenuation of the ‘fold’ catastrophe, when moving away from the critical point, as indicated by the fitted Airy curves (dotted lines, Fig. 3a,b). In contrast, the 22 eV harmonic remains flat, indicating that it cannot be associated with a spectral caustic. Clearly, the angular variation of the harmonics reveals the fundamental characteristics of the bright spectral features, independently validating their identification as caustics.

Fig. 3

Angular and temporal properties of the caustics.

a, Angular dependence of the 16.2 eV (purple circles) and 18.1 eV (blue circles) harmonics as a function of the crystal orientation. The angular dependence of each harmonic was shifted to zero at large angles away from the caustic and normalized to one. The dotted lines describe the fitted Airy function for 16.2 eV (purple dotted line) and 18.1 eV (blue dotted line), respectively (see Methods). The oscillation phase of the 16.2 eV (green squares) and 18.1 eV (pink squares) harmonics coincides in the vicinity of the caustics and separates beyond the enhanced angular region. To eliminate possible systematic errors, the presented oscillation phases are normalized by the phase of the 13.3 eV harmonic. **b**, Angular dependence for the 20 eV (red diamonds) and 22 eV (yellow triangles) harmonics, together with the fitted Airy function for the 20 eV harmonic (red dotted line). Both curves were shifted to zero and normalized according to the 20 eV harmonic. **c**, Theoretical values of the phase difference between the 16.2 eV and 18.1 eV harmonics (black squares) versus crystal orientation, along with the experimental phase difference (purple squares). The theory and experiment exhibit a remarkably similar trend as we rotate the crystal away from the singularity.

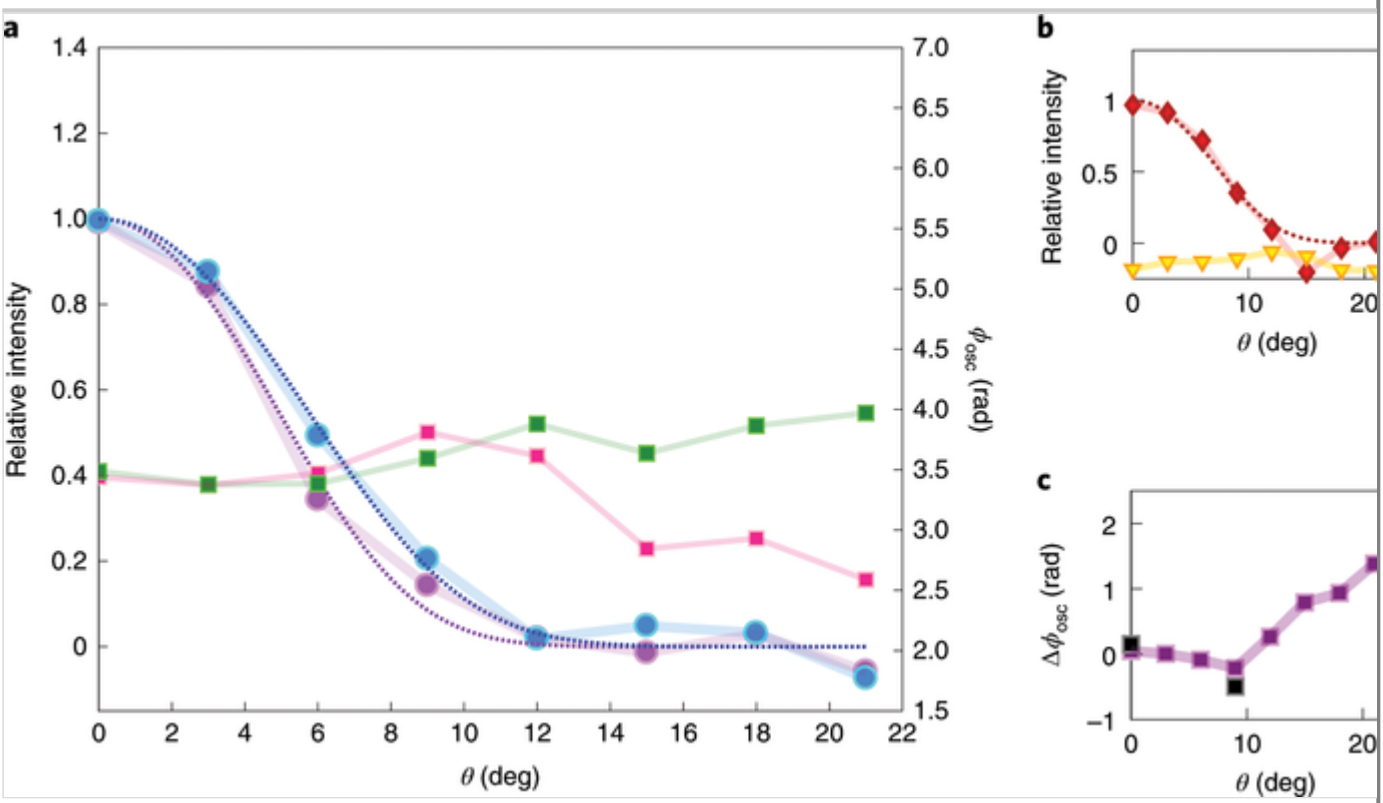

The lock-in measurement, induced by the second harmonic field, can be applied to reveal the dynamical properties of the electron–hole wavefunction in the vicinity of caustics. ~~Although~~While the The relation betwen the two parts of the sentence is addittion and not contrast. oscillation amplitude enables the identification of weak

signals, the oscillation phase serves as a sensitive probe of the internal dynamics[16, 27]. Figure 3a presents the oscillation phase of the 16.2 eV (green squares) and 18.1 eV (pink squares) harmonics, ~~respectively,~~ both of which originate at 0° from the X point singularity of the lowest conduction band (Fig. 2). At small angles, in the vicinity of the caustic, their oscillation phase coincides. As we increase the angle, and move away from the caustic, as is evident from the Airy attenuation of the enhancement their oscillation phase separates. The theoretical values of the phase difference between the 16.2 and 18.1 eV harmonics were calculated from 3D numerical simulations using the semiconductor Bloch equations. These values are plotted versus crystal orientation in Fig. 3c along with the experimental results, exhibiting a remarkably similar trend as we rotate the crystal and move away from the singularity. Far from the caustics the dynamics is dominated by semi-classical trajectories, where the phase separation reflects the trajectory modification with energy[16, 27]. In the vicinity of the caustics the semi-classical picture fails and the dynamics is dictated by the singularity in the dynamical JDOS. The clear difference in the oscillation phase between the two regions reveals that the attosecond electron–hole dynamics at the caustics and in the semi-classical regime are qualitatively distinct.

Finally, we note that the singularities are observed along the high-symmetry axes of the crystal; however, enhanced spectral features are observed at other angles as well, for example for the 20.5–22.5 eV region in Fig. 1c. Although the HHG signal is influenced by multiple parameters, such as dipole couplings (see Supplementary Information and Supplementary Fig. 5), the gaps between the conduction bands or their instantaneous excitation probabilities, many of the prominent spectral features can be understood through the dynamical JDOS. According to equation (5), valleys of low $\nabla_{\mathbf{k}}\varepsilon_{\mathrm{g}}(\mathbf{k})$ in the BZ lead to a spectral enhancement in the HHG signal, as observed in our experimental results (see Supplementary Information and Supplementary Fig. 6).

Conclusions

Our results establish the fundamental connection between the electronic structure of the crystal and the strong-field process. This study reveals how strong-field attosecond metrology serves as an extremely sensitive probe of ultrafast dynamical quantum interference between electron–hole wave packets in solids. We identify the important role of the dynamical JDOS, dictated by the strong-field nature of the interaction. As the dynamical JDOS becomes singular, the trajectory picture that governs the inter-band HHG process fails, giving rise to spectral caustics. The

mapping between the HHG spectrum and the bandgaps serves as unequivocal evidence of the dominant role of inter-band emission over numerous conduction bands. Looking forward, our study will form the framework for a wide range of attosecond-scale phenomena, where caustics will serve as sensitive probes of the strong-field modification of the band structure (see Supplementary Information and Supplementary Fig. 7). It will allow the study of ultrafast dynamics such as electron–hole interactions, leading to the formation of excitons, or electron–electron–phonon interactions. Furthermore, the control over sub-cycle electronic currents will play a role in the establishment of compact solid-state XUV sources, as well as in the field of petahertz electronics.

Methods

Experimental set-up

High harmonics were generated with a near-infrared laser source (Light Conversion Topas-HE) centred around a wavelength of 1.3 μm with a 1 kHz repetition rate and pulse duration of 50 fs. The beam was focused into a free-standing single crystal of MgO (<100>) with thickness of 100 μm. The intensity of the beam at the focus was ~1×10^{13} W cm^{-2}, which is just below the damage threshold of MgO. The orientation of the crystal axes with respect to the laser polarization was controlled by a rotation motor perpendicular to the beam propagation direction ($\theta = 0$ is determined by the HHG efficiency). The sample was placed inside a vacuum chamber in the imaging plane of the XUV grating. The second harmonic field, polarized perpendicular to the fundamental field, was generated using a 100 μm type I beta-barium borate (BBO, β-BaB_2O_4) crystal. Group-velocity dispersion was compensated using a birefringent crystal (calcite). The sub-cycle delay of the second harmonic relative to the fundamental field was controlled using a pair of fused-silica wedges. We recorded the harmonic spectra with an imaging XUV spectrometer consisting of a flat-field variable groove density grating and microchannel plates.

Airy function fit and calculation

Catastrophe theory predicts that a ‘fold’ catastrophe should take the shape of an Airy function as a function of the control parameters[24]. The parameter we changed in our experiment was the crystal orientation θ, but the explicit dependence of the HHG signal on θ is non-trivial. Catastrophe theory describes the signal in the vicinity of the singularity only, so in our fitting function we took the first non-vanishing order in θ (beyond the zero order). The HHG signal was

symmetric in θ around the high-symmetry axes of MgO, so the first non-vanishing order was θ^2, which is the control parameter appearing in the Airy function. As a result we applied the following fitting function in Fig. 3:

$$f(\theta) = \mathbf{a}\left|\mathrm{Airy}(\mathbf{b}\theta^2)\right|^2 + \mathbf{c}$$

where **a**, **b** and **c** are fitting parameters. We used a least-mean-square fitting algorithm, resulting in $R^2 > 0.985$ for all caustic harmonics.

Theoretical two-colour phase calculation

The numerical calculations were performed with the code described in ref. [32]. To calculate the field-free band structure and dipole couplings for MgO, we used the electronic structure code Quantum Espresso[33], with a Heyd–Scuseria–Ernzerhof exchange-correlation hybrid functional on a Monkhorst–Pack (MP) grid of $10 \times 10 \times 5$ points. We used a unit cell consisting of two slabs so that the *x* and *y* directions corresponded to the plane of polarization of the pulse, while the *z* direction corresponded to the direction of pulse propagation. This allowed us to use only a few points along the *z* direction for the posterior wave packet propagation. The bands were shifted to match the experimental bandgap using the so-called scissor operator[34].

The field-free tight-binding Hamiltonian used for the propagation was then constructed by projecting the Bloch bands onto a set of maximally localized Wannier functions using the Wannier90 code[35]. This procedure permitted us to obtain a consistent phase relation between orbitals, as explained in ref. [32]. The Bloch states were projected onto the sp^3d^2, d_{xy}, d_{xz} and d_{yz} orbitals of magnesium and the *p* orbitals of oxygen. The field-free Hamiltonian was then propagated in the presence of the field using the density matrix formalism.

To compute the amplitude and phase of the $4\omega_0$ oscillations (ω_0 is the frequency of the fundamental field), we used a two-colour field composed of a linearly polarized fundamental field at 1.3 μm in combination with its second harmonic polarized perpendicular to the fundamental field. Both pulses had a full-width at half-maximum of 30 fs. We performed 10 simulations for each angle, varying the relative carrier-envelope phases (CEP) between the ω and 2ω fields. We kept the ω field fixed and changed the CEP of the 2ω field from 0° to 180°. We then Fourier-transformed the oscillation of the harmonic intensity as a function of the CEP,

obtaining the 4ω oscillating amplitude and phase for each harmonic. For these simulations, we used a MP grid of $120 \times 120 \times 5$ k-points.

Online content

Any methods, additional references, Nature Research reporting summaries, source data, extended data, supplementary information, acknowledgements, peer review information; details of author contributions and competing interests; and statements of data and code availability are available at https://doi.org/10.1038/s41566-019-0574-4.

Supplementary information

Supplementary information is available for this paper at https://doi.org/10.1038/s41566-019-0574-4.

Publisher's note Springer Nature remains neutral with regard to jurisdictional claims in published maps and institutional affiliations.

Acknowledgements

N.D. is the incumbent of the Robin Chemers Neustein Professorial Chair. N.D. acknowledges financial support from the Minerva Foundation, the Israeli Science Foundation, the Crown Center of Photonics and the European Research Council. M.K. acknowledges financial support from the Minerva Foundation and the Koshland Foundation.

Author contributions

~~N.D. supervised the study.~~ N.D., A.J.U. and G.O. conceived and planned the experiments. A.J.U., G.O., V.B., T.A.-P. and B.D.B. performed the measurements. A.J.U. and G.O. analysed the data. A.J.U., G.O., A.J.-G., C.M., R.E.F.S., N.D.K., M.K., A.N.R., O.S., M.I., B.Y. and T.B. ~~worked on~~developed the theoretical models and analysis. All authors discussed the results and contributed to writing the manuscript.

Data availability

The data that support the findings of this study are available from the corresponding author upon reasonable request.

Supplementary information

Supplementary Information

Supplementary Figs. 1–7 and Discussion.

References

1. Ghimire, S. et al. Observation of high-order harmonic generation in a bulk crystal. *Nat. Phys.* **7**, 138–141 (2011).

2. Vampa, G. et al. All-optical reconstruction of crystal band structure. *Phys. Rev. Lett.* **115**, 193603 (2015).

3. Luu, T. T. et al. Extreme ultraviolet high-harmonic spectroscopy of solids. *Nature* **521**, 498–502 (2015).

4. Garg, M. et al. Multi-petahertz electronic metrology. *Nature* **538**, 359–363 (2016).

5. Liu, H. et al. High-harmonic generation from an atomically thin semiconductor. *Nat. Phys.* **13**, 262–265 (2017).

6. Yoshikawa, N., Tamaya, T. & Tanaka, K. High-harmonic generation in graphene enhanced by elliptically polarized light excitation. *Science* **356**, 736–738 (2017).

7. Hohenleutner, M. et al. Real-time observation of interfering crystal electrons in high-harmonic generation. *Nature* **523**, 572–575 (2015).

8. Ndabashimiye, G. et al. Solid-state harmonics beyond the atomic limit. *Nature* **534**, 520–523 (2016).

9. You, Y. S. et al. High-harmonic generation in amorphous solids. *Nat. Commun.* **8**, 724 (2017).

10. You, Y. S. et al. Laser waveform control of extreme ultraviolet high harmonics from solids. *Opt. Lett*. **42**, 1816–1819 (2017).

11. Hawkins, P. G., Ivanov, M. Y. & Yakovlev, V. S. Effect of multiple conduction bands on high-harmonic emission from dielectrics. *Phys. Rev. A* **91**, 013405 (2015).

12. Silva, R., Blinov, I. V., Rubtsov, A. N., Smirnova, O. & Ivanov, M. High-harmonic spectroscopy of ultrafast many-body dynamics in strongly correlated systems. *Nat. Photon.* **12**, 266–270 (2018).

13. Vampa, G., McDonald, C., Orlando, G., Corkum, P. & Brabec, T. Semiclassical analysis of high harmonic generation in bulk crystals. *Phys. Rev. B* **91**, 064302 (2015).

14. Ashcroft, N. W. & Mermin, N. D. in *Solid State Physics* 144–145 (Holt, Rinehart and Winston, 1976).

15. Van Hove, L. The occurrence of singularities in the elastic frequency distribution of a crystal. *Phys. Rev.* **89**, 1189–1193 (1953).

16. Vampa, G. et al. Linking high harmonics from gases and solids. *Nature* **522**, 462–464 (2015).

17. Schubert, O. et al. Sub-cycle control of terahertz high-harmonic generation by dynamical Bloch oscillations. *Nat. Photon.* **8**, 119–123 (2014).

18. Kemper, A., Moritz, B., Freericks, J. & Devereaux, T. Theoretical description of high-order harmonic generation in solids. *New J. Phys.* **15**, 023003 (2013).

19. Higuchi, T., Stockman, M. I. & Hommelhoff, P. Strong-field perspective on high-harmonic radiation from bulk solids. *Phys. Rev. Lett.* **113**, 213901 (2014).

20. Vampa, G. et al. Theoretical analysis of high-harmonic generation in solids. *Phys. Rev. Lett.* **113**, 073901 (2014).

21. Golde, D., Meier, T. & Koch, S. High harmonics generated in semiconductor nanostructures by the coupled dynamics of optical inter- and intraband excitations. *Phys. Rev. B* **77**, 075330 (2008).

22. Tancogne-Dejean, N., Mücke, O. D., Kärtner, F. X. & Rubio, A. Impact of the electronic band structure in high-harmonic generation spectra of solids. *Phys. Rev. Lett.* **118**, 087403 (2017).

23. Raz, O., Pedatzur, O., Bruner, B. D. & Dudovich, N. Spectral caustics in attosecond science. *Nat. Photon.* **6**, 170–173 (2012).

24. Upstill, C. & Berry, M. IV Catastrophe optics: morphologies of caustics and their diffraction patterns. *Prog. Optics* **18**, 257–346 (1980).

25. You, Y. S., Reis, D. A. & Ghimire, S. Anisotropic high-harmonic generation in bulk crystals. *Nat. Phys.* **13**, 345–349 (2017).

26. Wu, M. et al. Orientation dependence of temporal and spectral properties of high-order harmonics in solids. *Phys. Rev. A* **96**, 063412 (2017).

27. Bruner, B. D. et al. Multidimensional high harmonic spectroscopy. *J. Phys. B* **48**, 174006 (2015).

28. Li, J.-B. et al. Enhancement of the second plateau in solid high-order harmonic spectra by the two-color fields. *Opt. Express* **25**, 18603–18613 (2017).

29. Ehrenreich, H. & Philipp, H. Optical properties of Ag and Cu. *Phys. Rev.* **128**, 1622–1629 (1962).

30. Roessler, D. & Walker, W. Electronic spectrum and ultraviolet optical properties of crystalline MgO. *Phys. Rev.* **159**, 733–738 (1967).

31. Faccialà, D. et al. Probe of multielectron dynamics in xenon by caustics in high-order harmonic generation. *Phys. Rev. Lett.* **117**, 093902 (2016).

32. Silva, R., Martín, F. & Ivanov, M. High harmonic generation in crystals using maximally localized Wannier functions. Preprint at https://arxiv.org/abs/1904.00283 (2019).
AQ11

33. Giannozzi, P. et al. Quantum espresso: a modular and open-source software project for quantum simulations of materials. *J. Phys.* **21**, 395502 (2009).

34. Levine, Z. H. & Allan, D. C. Linear optical response in silicon and germanium including self-energy effects. *Phys. Rev. Lett.* **63**, 1719–1722 (1989).

35. Mostofi, A. A. et al. An updated version of Wannier90: a tool for obtaining maximally-localised Wannier functions. *Comput. Phys. Commun.* **185**, 2309–2310 (2014).